RSC Advances

ROYAL SOCIETY OF CHEMISTRY

www.rsc.org/advances

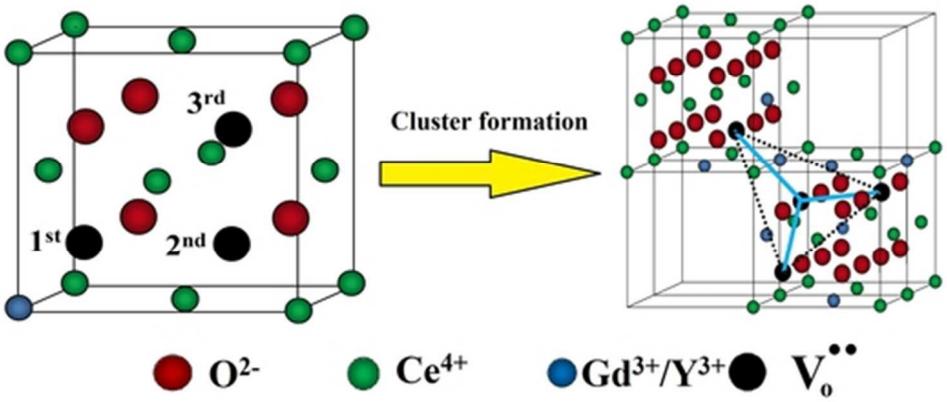

Defect cluster formation in nanoceria due to doping
23x10mm (600 x 600 DPI)

Charge carrier dynamics in Gd-Y co-doped nanocrystalline ceria corroborated with defect interactions

Sk Anirban[a,b] and Abhigyan Dutta[a,*]

[a] Department of Physics, The University of Burdwan, Burdwan-713104, India

[b] Department of Physics, Govt. General Degree College, Singur, Hooghly-712409, India

Abstract

Defect associates and their interactions with charge carriers, influencing the ion dynamics have been discussed for Gd^{3+} and Y^{3+} co-doped nanocrystalline ceria. Detailed Rietveld analysis of the X-Ray Diffraction data confirmed the single phase cubic fluorite structure of the compositions with space group $Fm\bar{3}m$. An overall increase of lattice parameter with Gd^{3+} ions concentration has been found. Grain and specific grain boundary conductivity have been evaluated from the complex impedance plots. A higher value of dielectric constant has been observed for co-doped sample at 20 mol % doping concentration. The interaction between dopant cations with oxygen vacancies has been found to form different defect associates and defect clusters. The association energy of co-doped samples at 20 mol % doping concentration is observed to be minimum in comparison with the singly doped samples of same concentration. It has also been found that different defect clusters have a significant role on ionic conduction. The correlation among structural parameters, dielectric and conductivity response has been discussed and established.

***Author for correspondence: A. Dutta**

Address: Department of Physics, The University of Burdwan, Golapbag, Burdwan-713104, INDIA email: adutta@phys.buruniv.ac.in **; Telephone: +913422657800; Fax: +91342 2634015**

1. Introduction

It is well known that, doped ceria fluorites are better ionic electrolyte material for operation in intermediate temperature solid oxide fuel cells than conventional yttria-stabilized zirconia (YSZ)[1]. Although, pure ceria is not a good ionic conductor, but with the doping of aliovalent cation into the ceria lattice, the ionic conductivity increases significantly[2-6]. This is because lower valence cations into the ceria lattice can generate defects like dopants and oxygen vacancies which has strong influence in ion conduction. In doped ceria, normally, the oxygen ions carry current by oxygen vacancy hoping mechanism[7]. Earlier studies[8] showed that, ceria doped with trivalent rare earth ions, gives higher ionic conductivity than those doped with other elements. The major problem of these solid electrolytes is the increase of electronic conductivity at low oxygen partial pressure and high temperature because of Ce^{4+} to Ce^{3+} reduction during the reaction from $Ce^{4+}O_2$ to $Ce_{1-x}{}^{4+}Ce_x{}^{3+}O_{2-x/2}$. One of the possible ways to overcome this problem is the use of co-doping which suppress the ordering of oxygen vacancy and therefore lower the activation energy of conduction and improve ionic conductivity[9]. The oxygen ion transport behavior in oxygen-ion conductors is mainly dominated by the association effects of dopant cations and accompanied oxygen vacancies[10]. Co-doping with appropriate ratio of gadolinium and yttrium in ceria can be used as an ideal electrolyte material of IT-SOFCs[11]. The ionic conductivity of these ceria based electrolytes strongly depend on doping concentration, ionic radius of dopant, number of oxygen vacancies, grain size, impurity segregation and inhomogeneity inside the grain[8-12]. In these ionic conductors, the conductivity varies linearly

with the oxygen vacancy concentration for lower doping concentration but at higher doping concentration, the ionic conductivity usually exhibits a nonlinear dependence[13]. This is due to defect interactions, clustering or ordering of oxygen vacancy at different doping concentration[14-15]. Generally, oxygen vacancies associated with dopant cations, form defect cluster and dissociate from defect associate or cluster during the conduction process[16]. These defect clusters contains one or more oxygen vacancies. The columbic interaction between oxygen vacancy and dopant cations plays a major role in ionic conduction and the values of lattice parameter and dielectric constant mainly control the association energy of oxygen vacancy[17]. There are several literatures on the conductivity of singly and co-doped ceria concerning activation energy and lattice strain, but very few of them discussed effect of defect associate on the ionic conductivity of co-doped ceria. The effect of dielectric constant and defect clusters on the conductivity of co-doped ceria is not clear until now. The main aim of this work is to investigate the formation of defect clusters due to co-doping and their influence on the ion dynamics of these materials.

2. Theory of defect clusters

In this section, we discuss the defect theory and formation of defect cluster for rare earth (RE) doped ceria. Generally, it is assumed that, the charge compensating defects produced by doping ceria with cations that have a lower valency than the cerium ions results in the formation of oxygen vacancies[13]. Therefore when RE ions are doped into ceria then one oxygen vacancy is formed for every two RE ions for charge neutrality which is well presented by the Kröger – Vink notation:

$$RE_2O_3 + 2CeO_2 \rightarrow 2RE'_{Ce} + 3O^x_o + V^{\bullet\bullet}_o \quad (1)$$

Here RE'_{Ce} indicates one Ce^{4+} site occupied by RE^{3+} ion, $V_o^{\bullet\bullet}$ is the oxygen vacancy. There is another type of mechanism by which oxygen vacancies are also created due to the doping of RE ions in the ceria lattice which may be depicted as,

$$2RE_2O_3 \xrightarrow{CeO_2} 3RE'_{Ce} + RE_i^{\cdots} + 6O_o^x \quad (2)$$

These two mechanisms are referred as vacancy compensation (Eqn 1) and dopant compensation mechanism (Eqn 2) respectively. According to M. Nakayama et al.[18], majority of oxygen vacancies are created by vacancy compensation mechanism due to the much smaller solution energy of Eqn (1) compared to Eqn (2). In our present study, we have considered only the oxygen vacancy creation by vacancy compensation mechanism. The created oxygen vacancies being positively charged associate with RE^{3+} ions to form *dopant-vacancy associates*. There are several relative positions between dopant cations and oxygen vacancies in ceria lattice. Fig. 1 illustrates these positions of RE dopant to an oxygen vacancy at first, second and third neighbor site within the cubic fluorite unit cell. RE dopant cations prefer to occupy the first or second neighbor sites with respect to their related vacancies[19]. Dopant with smaller ionic radii is energetically favorable for the vacancy to the first neighbor position and dopant with larger ionic radii prefer second neighbor vacancies. It was earlier shown that[20] a variety of defect associates and cluster configuration of the rare earth doped ceria involving oxygen vacancies are located at either the first or the second neighbor site to the corresponding dopant. Columbic interaction between dopant cation and oxygen vacancy plays a major role for the formation of defect associates and clusters. However, columbic interaction favours the first neighbor site and the relaxation energy favours the second neighbor site[19]. Fig. 2 shows the different defect cluster configurations with oxygen vacancies occupying the first neighbor site to the associate dopant. This figure shows the defect cluster configuration of oxygen vacancies ranging from $1V_o^{\bullet\bullet}$ to

$6V_O^{\bullet\bullet}$. The defect cluster configurations ($3V_O^{\bullet\bullet}-6RE'_{Ce}$) and ($6V_O^{\bullet\bullet}-12RE'_{Ce}$) have highest binding energy among all other different defect cluster configurations[20]. According to Z. P. Li et al.[21], ($6V_O^{\bullet\bullet}-12RE'_{Ce}$) defect cluster configuration can be considered as building block for the development of large defect cluster due to its high symmetric and unique dumbbell like structure. The defect cluster configuration with oxygen vacancies occupying the second neighbor site to the associate dopants also shows the similar configuration as shown in Fig. 2. In the stable configuration of large defect cluster in co-doped ceria different dopant cations in the cluster prefer segregation to a mixture in the cluster and smaller dopant cations favours the outer region of the cluster due to reduced elastic strain around the defect clusters[22]. For low doping concentration, defect pair ($1V_O^{\bullet\bullet}-1RE'_{Ce}$) and smallest neutralized trimers ($1V_O^{\bullet\bullet}-2RE'_{Ce}$) are distributed throughout the ceria lattice. Large defect clusters are formed at higher doping concentration and also in singly doped ceria. This growth of defect cluster can be restrained by the co-doping effect i.e. co-doped materials promotes the growth of small defect cluster like ($1V_O^{\bullet\bullet}-2RE'_{Ce}$) and ($2V_O^{\bullet\bullet}-4RE'_{Ce}$). Energetically neutral trimers are qualitatively similar to the charger dimer[19]. Again two oxygen vacancies can form defect associate like ($V_O^{\bullet\bullet}-V_O^{\bullet\bullet}$). All the above defect associates give a negative effect on oxygen ion conduction due to the trapping of oxygen vacancies by the rare earth ions or due to a correlated motion of oxygen vacancies repelling each other. Large defect cluster means more the trapping effect and consequently lower conductivity[23-24]. The defect associate ($V_O^{\bullet\bullet}-V_O^{\bullet\bullet}$) is significant because during the conduction process, we need to consider at least one oxygen vacancy distributed in the next nearest neighbor site that affects oxygen vacancy jumps to the nearest neighbor sites[18]. Nevertheless, it is energetically stable for the formation of two isolated oxygen vacancies rather than the formation of oxygen vacancy defect associate.

3. Materials and methods

The nanocrystalline $Ce_{0.9}Gd_{0.1-x}Y_xO_{1.95}$ ($0 \leq x \leq 0.1$) and $Ce_{0.8}Gd_{0.2-y}Y_yO_{1.9}$ ($0 \leq y \leq 0.2$) (hereafter abbreviated as GDY1 and GDY2 respectively) materials were prepared through the low temperature citrate auto-ignition method. $Ce(NO_3)_3.6H_2O$ (99.9%), Gd_2O_3 (99.9%) and Y_2O_3 (99.9%) were used as starting materials. The sample preparation technique has been discussed in our earlier work[25]. The as prepared powdered samples were annealed at 400^{o}C for 2 hours then again sintered at 800^{o}C for 6 hours. During annealing/sintering the rise in temperature was in rate 5 ^{o}C/min. and the cooling was normal furnace cooling. X-ray diffraction measurements were performed (Bruker, model D8 Advance – AXS) using Cu K_α radiation. Diffraction data were recorded in a 2θ range from 20° to 80° in 0.02° steps. Cylindrical pellets were prepared from sintered powder by uniaxial pressing in a 10 mm diameter stainless steel die. Graphite paste was applied to both faces of the pellets to make the necessary electrode. The electrical measurements were performed in a tube furnace using two probe methods in air atmosphere. An LCR meter (HOIKI, Model 3532-50) interfaced with PC, was used to collect the electrical data in the frequency range 42 Hz to 5 MHz and in the temperature range 250^{0}C to 550^{0}C.

4. Results and discussion

4.1 X-Ray Diffraction and Rietveld Analysis

The formed phases and structural parameters of the sintered powder were investigated using XRD data. The crystal structure and phase purity of Gd, Y and Gd-Y co-doped ceria were confirmed by XRD analysis. For microstructural analysis of the sintered nanopowders, the Rietveld structure refinement process has been employed using MAUD software (version 2.33). The Marquardt least-squares procedure is adopted for minimization of the difference between the

observed and simulated powder diffraction patterns and the minimization is monitored using the reliability index parameter, such as weighted residual error (R_{wp}) and expected error (R_{exp}). This leads to the value of goodness of fit (GoF):

$$\text{GoF} = \frac{R_{wp}}{R_{exp}} \quad (3)$$

A good refinement is represented by low values of these parameters: R_{wp} around 0.10 for XRD in a conventional diffractometer, and GoF around 1.[26] Fig. 3(a) shows the Rietveld refined XRD patterns of all the samples. To make it more clear and visible, we have given the Rietveld refinement output for the sample y = 0.1 in Fig. 3(b). No additional peaks due to Gd and Y are present in the diffraction patterns that prove the complete dissolution of Gd and Y into the host ceria lattice. The observed peaks in the XRD patterns are well indexed and consistent with the reference data [JCPDS file: 34-03940]. The Rietveld analysis also confirms the single phase cubic fluorite structure with space group $Fm\bar{3}m$ of the materials. Different structural parameters obtained after Rietveld refinement are listed in Table 1. This table shows that RMS strain shows a maximum value for the co-doped samples in both GDY1 and GDY2 system. The particle size is in the range 12.08 nm - 21.77 nm which confirms the successful formation of nanostructures in citrate auto-ignition method. In both the systems, it has been observed that, the lattice parameter increases with the concentration of Gd^{3+} ions. This is due to fact that, ionic radius of Gd^{3+} (1.053Å) is greater than Y^{3+} (1.019Å). Again in the singly Gd^{3+} or Y^{3+} doped samples the lattice parameter increases with the total dopant concentration. This is because ionic radius of both Gd^{3+} and Y^{3+} is greater than the ionic radius of Ce^{4+} ions (0.97Å). The co-doped sample of GDY2 system shows a lower value of lattice parameter than the GDY1 system. This may due to higher columbic interaction between dopant cations and oxygen vacancy in co-doped sample of GDY2 system in comparison with GDY1 system, which reduces the lattice parameter. The variation

Ce–O bond length shows the same trend as lattice parameter i.e co-doped samples have higher values than the singly doped samples.

4.2 Dielectric Properties

Dielectric constant of a defect system has a major role in the ionic conductivity as it controls the columbic interaction between dopant ions and oxygen vacancies and the formation of defect clusters. Therefore, to investigate the ionic conduction of GDY1 and GDY2 system, the knowledge of dielectric constant should be necessary. We have evaluated the dielectric constant of these systems from the real part of the frequency dependent complex dielectric spectra using generalized Havriliak-Negami (HN) formalism[27]. The generalized dielectric function is given by,

$$\varepsilon^*(\omega) = \varepsilon'(\omega) - i\varepsilon''(\omega) = \varepsilon_\infty + \frac{\varepsilon_s - \varepsilon_\infty}{[1+(i\omega\tau_{HN})^\alpha]^\beta} \quad (4)$$

Where ε_s and ε_∞ are the relaxed and unrelaxed (dielectric constant) permittivity respectively, τ_{HN} is the characteristic relaxation time and α and β are the shape parameters satisfying the condition $0 \leq \alpha \leq 1$ and $0 \leq \alpha\beta \leq 1$. The frequency variation of $\varepsilon'(\omega)$ for all the samples are shown in Fig. 4(a). The real part of HN equation has been fitted to the real part of the complex dielectric spectra. The value of different parameters obtained after HN fit are listed in Table 2. This table reveals that the dielectric constant of GDY1 system is comparatively higher than GDY2 system. The dielectric constant of GDY1 system increases with the Gd^{3+} content and co-doped sample of GDY2 system shows higher value of dielectric constant than the singly doped sample. The variation of dielectric constant of the co-doped samples of GDY1 and GDY2 system with temperature is shown in Fig. 4(b) which reveals an increase in dielectric constant with measuring temperature. The temperature variation of dielectric constant of other samples shows the same behavior. This increase of dielectric constant with temperature is due to the increase of

polarization of charge carriers with temperature. The temperature variation of τ_{HN} is shown in Fig. 4(c) which obeys the conventional Arrhenius relation and the corresponding activation energies are listed in Table 2. The activation energy of the co-doped sample of the system GDY1 shows higher value than the singly doped samples but at higher concentration (GDY2 system) it shows an opposite behavior. The variation of shape parameters with temperature of the sample *y* = 0.1 are shown in Fig. 4(d). The shape parameter of the other samples shows similar nature. It should be noted that the values of α and β increases slightly with temperature i.e. the shape of the real part of dielectric spectra is weakly thermally activated.

Fig. 5 illustrate the frequency dependence of dielectric loss tangent for the sample *y* = 0.2 at different temperatures. This figure shows the existence of a single relaxation peak which is attributed to the dipole moment of the defect pair like $(RE'_{Ce}-V_0^{\bullet\bullet})^{\bullet}$ formed due to the association of oxygen vacancy with one of the trivalent dopant cations. The relaxation peak at frequency ω_{max} shifts towards the higher frequency side and the intensity of the relaxation peak increases with the temperature. The increase of relaxation peak intensity with temperature is due to the increase of free oxygen vacancies which are released from the defect associates. Generally, the oxygen vacancies are associated with the dopant cations to form defect associate and defect clusters. Therefore some energy is required to create free oxygen vacancies from defect associates and defect clusters. This energy is the dissociation energy of an oxygen vacancy, same as the association energy of oxygen vacancies with the dopant cations. This association energy can be calculated from the slope of the Arrhenius plot of $\log[T(\tan\delta_{max})]$ vs 1/T. The Arrhenius plot of $\log[T(\tan\delta_{max})]$ vs 1/T for the sample *y* = 0.2 in the temperature range is shown in the inset of Fig. 5. This Arrhenius plot shows two slopes, one in the temperature range 325 ^{o}C-400^{o}C and another is in the range 400 ^{o}C-550^{o}C. The association energies in this two temperature

ranges are 0.20 eV and 0.12 eV respectively. Therefore at low temperature, the oxygen vacancies are strongly associated with dopant cations and this association decreases at higher temperature. This strong association of oxygen vacancies with dopant cations at low temperature was also observed in others samples. Thus due to low dopant-vacancy association at high temperatures we mainly consider the association energy at higher temperature range. The association energy for all the samples is listed in Table 3. It may be noted that the association energy of GDY1 system increases with the Y^{3+} dopant concentration but the co-doped sample of the GDY2 system shows minimum association energy than the solely doped samples.

4.3 Electrical conductivity

To investigate the effect of dielectric constant and defect association on ionic conduction, we have calculated the dc conductivity of the samples using Nyquist plots. Fig. 6(a) shows the typical Nyquist plot for all the samples at 525^{o}C. The high frequency and low frequency semi circular arcs correspond to grain and grain boundary contributions respectively[25]. The presence of two semicircular arcs indicates both the grain and grain boundary are involved in over all conduction process. The values of grain and specific grain boundary conductivity of each sample has been calculated and listed in Table 3. It has been found that the grain conductivity is roughly 1-2 orders of magnitude higher than the specific grain boundary conductivity. The temperature dependence of grain conductivity is shown on Fig. 6(b) which shows the continuous increase of conductivity with temperature. The small conductivity at low temperature is due to the of defect associates which are formed due to the columbic interaction between dopant cations and oxygen vacancies given by

$$F = \left| \frac{-2e^2}{4\pi\varepsilon_o\varepsilon_\infty r^2} \right| \quad (5)$$

Where ε_∞ is the dielectric constant and r is the inter-ionic distance between dopant cations and oxygen vacancy and with the increase of lattice parameter it is expected to increase r. In our present study we have considered the defect associates $(V_0^{\bullet\bullet} - V_0^{\bullet\bullet})$ and $(RE'_{Ce} - V_0^{\bullet\bullet})^{\bullet}$ and defect cluster ranging from $(1V_0^{\bullet\bullet} - 2RE'_{Ce})$ to $(6V_0^{\bullet\bullet} - 12RE'_{Ce})$. As we have discussed earlier that, the conductivity increases with temperature which is due to increase of dielectric constant with temperature. With the increase of dielectric constant the columbic interaction decreases according to Equation 5. Therefore oxygen vacancies dissociates from defect associates described as:

$$(V_0^{\bullet\bullet} - V_0^{\bullet\bullet}) \leftrightarrow 2V_0^{\bullet\bullet} \quad (6)$$

$$(RE'_{Ce} - V_0^{\bullet\bullet})^{\bullet} \leftrightarrow V_0^{\bullet\bullet} + RE'_{Ce} \quad (7)$$

$$(1V_0^{\bullet\bullet} - 2RE'_{Ce}) \leftrightarrow V_0^{\bullet\bullet} + 2RE'_{Ce} \quad (8)$$

$$(2V_0^{\bullet\bullet} - 4RE'_{Ce}) \leftrightarrow (V_0^{\bullet\bullet} + 2RE'_{Ce}) + V_0^{\bullet\bullet} + 2RE'_{Ce} \leftrightarrow 2V_0^{\bullet\bullet} + 4RE'_{Ce} \quad (9)$$

$$(3V_0^{\bullet\bullet} - 6RE'_{Ce}) \leftrightarrow (2V_0^{\bullet\bullet} + 4RE'_{Ce}) + V_0^{\bullet\bullet} + 2RE'_{Ce} \leftrightarrow 3V_0^{\bullet\bullet} + 6RE'_{Ce} \quad (10)$$

$$(4V_0^{\bullet\bullet} - 8RE'_{Ce}) \leftrightarrow (3V_0^{\bullet\bullet} + 6RE'_{Ce}) + V_0^{\bullet\bullet} + 2RE'_{Ce} \leftrightarrow 4V_0^{\bullet\bullet} + 8RE'_{Ce} \quad (11)$$

$$(5V_0^{\bullet\bullet} - 10RE'_{Ce}) \leftrightarrow (4V_0^{\bullet\bullet} + 8RE'_{Ce}) + V_0^{\bullet\bullet} + 2RE'_{Ce} \leftrightarrow 5V_0^{\bullet\bullet} + 10RE'_{Ce} \quad (12)$$

$$(6V_0^{\bullet\bullet} - 12RE'_{Ce}) \leftrightarrow (5V_0^{\bullet\bullet} + 10RE'_{Ce}) + V_0^{\bullet\bullet} + 2RE'_{Ce} \leftrightarrow 6V_0^{\bullet\bullet} + 12RE'_{Ce} \quad (13)$$

Here RE is either Gd or Y. Thus with the increase of temperature oxygen vacancy dissociates from defect associates and the concentration of oxygen vacancy increases and in turn ionic conductivity increases. These oxygen vacancies dissociated from defect associates, assist the migration of oxygen ions in conduction process. In the low temperature regime, the association

energy of all the samples is high compare to high temperature regime. In GDY1 system, the main defect associates are $(V_0^{\bullet\bullet} - V_0^{\bullet\bullet})$, $(RE'_{Ce} - V_0^{\bullet\bullet})^{\bullet}$ and $(1V_0^{\bullet\bullet} - 2RE'_{Ce})$ for lower doping concentration. In GDY2 system all of the defect associates and clusters have a significant effect in conductivity. Table 2 shows that GDY1 system has high dielectric constant than GDY2 system i.e. columbic interaction between dopant cations and oxygen vacancies is low at lower dopant concentration. This interaction is more significant at higher dopant concentration. Although due to lower interaction in GDY1, it shows lower conductivity than GDY2. This abnormality is due to the oxygen vacancy concentration. The oxygen vacancy concentration in $Ce_{1-z}RE_zO_{2-z/2-\delta}$ (where $CeO_{2-\delta}$ is doped with rare earth oxide and $z>\delta$) is given by[13]

$$[V_0^{\bullet\bullet}] = \frac{2z}{a^3} \qquad (14)$$

Here 'a' is the lattice parameter. Therefore the oxygen vacancy concentration in GDY2 system is greater than GDY1 system (as z =0.2 for GDY2 and z =0.1 for GDY1) and consequently GDY2 shows higher conductivity than GDY1. In GDY1 system, co-doped sample shows lower conductivity than singly doped samples. This is because in co-doped sample of GDY1, oxygen vacancy concentration is lower than singly doped samples because of its higher lattice parameter. In GDY1 system, single Gd^{3+} doped sample shows higher conductivity than others do due to its high dielectric constant and low columbic interaction. The variation of association energy and conductivity of the system GDY1 is shown in Fig. 7(a). In the GDY2 system the ionic conductivity is strongly related to dielectric constant and interaction between dopant cations and oxygen vacancies. Lattice parameter of GDY2 system increases linearly with Gd^{3+} ions concentration. Hence, according to Equation 14, oxygen vacancy decreases. But the Gd^{3+} doped samples show high conductivity than Y^{3+} doped samples due to is high dielectric constant and

low columbic interaction. The co-doped sample in GDY2 system shows higher dielectric constant, thus lower columbic interaction i.e. oxygen vacancy easily dissociates from defect associates and clusters in co-doped samples and as a result higher conductivity appears. As discussed earlier, the defect clusters $(3V_0^{\bullet\bullet} - 6RE'_{Ce})$ and $(6V_0^{\bullet\bullet} - 12RE'_{Ce})$ have highest binding energy. The presence of these clusters may decrease the ionic conduction of singly doped samples. The main advantage of co-doped sample is that they prevent the formation of these types of large clusters. Only small defect clusters are formed in the co-doped samples. As a result the co-doped sample of GDY2 system shows lower association energy than the solely doped samples. Therefore the oxygen vacancies can easily dissociates from defect clusters. The variation of association energy and conductivity of the system GDY2 is shown in Fig. 7(b) which reveals that the sample y = 0.1 shows lower association energy and higher conductivity.

5. Conclusions

In summary, the GDY1 and GDY2 nanomaterials were prepared by low temperature citrate auto –ignition method. Rietveld analysis of the XRD data confirmed the single phase cubic fluorite structure of the materials. The impedance spectra confirmed the contribution of grain and grain boundary to the total conductivity. It had been found that, the dielectric constant playes a major role in columbic interaction between dopant cations and oxygen vacancies. The oxygen vacancy concentration increased with temperature due to dissociation of oxygen vacancies from defect clusters. The large defect clusters had a negative effect on ionic conduction at higher doping concentration. In both GDY1 and GDY2 system, the conductivity was found to be controlled by dielectric constant and oxygen vacancy concentration. Also, the co-doped samples of GDY2 system suppressed the formation of large and stable defect clusters.

Acknowledgements

One of the authors (AD) thankfully acknowledges the financial assistance from Department of Science and Technology (Govt. of India) (Grant no: SR/FTP/PS-141-2010). The authors also acknowledge the instrumental support from DST (Govt. of India) under departmental FIST programme (Grant no: SR/FST/PS-II-001/2011) and University Grants Commission (UGC) for departmental CAS (Grant no. F.530/5/CAS/2011(SAP-I)) scheme.

Reference

1 B.C.H. Steele, *Solid State Ionics*, 2000, **129**, 95-110.

2 H. Arai, T. Kunisaki, Y. Shimizu and T. Seiyama, *Solid State Ionics*, 1986, **20**, 241-248.

3 K. C. Anjaneya, G. P. Nayaka, J. Manjanna, G. Govindaraj and K. N. Ganesha, *J. Alloys and Compd.*, 2013, **578**, 53-59.

4 N. Jaiswal, D. Kumar, S. Upadhyay and O. Prakash, *J. Power Sources*, 2013, **222**, 230-236.

5 S. J. Hong, K. Mehta and A. V. Virkar, *J. Electrochem. Soc*., 1998, **145**, 638-647.

6 M. Dudek, *J. European Ceram. Soc*., 2008, **28**, 965-971.

7 Raghvendra, R. K. Singh and P. Singh, *J. Mater. Sci*., 2014, **49**, 5571–5578.

8 H. Inaba and H. Tagawa, *Solid State Ionics*, 1996, **83**, 1-10.

9 H. Yamamura, E. Kotah, M. Ichikawa, K. Kakinuma, T. Mori and H. Haneda, *Electrochem*., 2000, **68**, 455-459.

10 D. Schneider, M. Godickemeier and L.J. Gauckler, *J. Electroceramics*, 1997, **1**, 165-172.

11 X. Guan, H. Zhou, Y. Wang and J. Zhang, *J. Alloys and Compd*., 2008, **464**, 310-316.

12 D. R. Ou, T. Mori, F. Ye, J. Zou and J. Drennan, *Renewable Energy*, 2008, **33**, 197-200.

13 R. T. Dirstine, R. N. Blumenthal and T. F. Kuech, *J. Electrochem. Soc*., 1979, **126**, 264-269.

14 J. M. de Souza e Silva, M. Strauss, C. M. Maroneze, E. R. Souza, Y. Gushikem, F. A. Sigoli and I. O. Mazali, *J. Mater. Chem*., 2011, **21**, 15678-15685.

15 Z. P. Li, T. Mori, F. Ye, D. Ou, G. Auchterlonie, J. Zou and J. Drennan, *J. Phys. Chem. C*, 2012, **116**, 5435-5443.

16 K. P. Padmasree, R. A. Montalvo-Lozano, S. M. Montemayor and A. F. Fuents, *J. Alloys and Compd.*, 2011, **509**, 8584-8589.

17 A. K. Baral and V. Sankaranarayanan, *J. Electrochem. Soc*., 2010, **157**, 53-58.

18 M. Nakayama and M. Martin, *Phys. Chem. Chem. Phys*., 2009, **11**, 3241-3249.

19 L. Minervini, M.O. Zacate and R.W. Grimes, *Solid State Ionics*, 1999, **116**, 339-349.

20 Z.P. Li, T. Mori, J. Zou and J. Drennan, *Phys. Chem. Chem. Phys*., 2012, **14**, 8369-8375.

21 Z.P. Li, T. Mori, F. Ye, D.R. Ou and J. Drennan, *J. Chem. Phys*., 2011, **134**, 224708.

22 D.R. Ou, F. Ye and T. Mori, *Phys. Chem. Chem. Phys*., 2011, **13**, 9554-9560.

23 J.A. Kilner, *Chem. Lett*., 2008, **37**, 1012-2015.

24 B. Wang, R.J. Leuis and A.N. Cormack, *Acta. Mater*., 2011, **59**, 2035-2045.

25 Sk. Anirban, T. Paul, P. T. Das, T. K. Nath and A. Dutta, *Solid State Ionics*, 2015, **270**, 73-83.

26 L.B. Mc Cusker, R.B. Von Dreele, D.E. Cox, D. Louer and P. Scardi, *J. Appl. Cryst*., 1999, **32**, 36-50.

27 S. Havriliak and S. Negami, *Polymer*, 1967, **8**, 161-210.

Figure captions:

Fig.1 Crystal structure of defect fluorite-type ceria with oxygen vacancy located at the 1st, 2nd and 3rd neighbor sites with respect to associated dopant cations. The green sphere represents Ce^{4+} ions, red sphere represents O^{2-} ions, blue sphere represents RE^{3+} ions and black sphere represents oxygen vacancies $V_0^{\bullet\bullet}$.

Fig. 2 The different defect cluster configuration with oxygen vacancies **(a)** $(1V_0^{\bullet\bullet} - 2RE_{Ce}^{'})$, **(b)** $(2V_0^{\bullet\bullet} - 4RE_{Ce}^{'})$, **(c)** $(3V_0^{\bullet\bullet} - 6RE_{Ce}^{'})$, **(d)** $(4V_0^{\bullet\bullet} - 8RE_{Ce}^{'})$, **(e)** $(5V_0^{\bullet\bullet} - 10RE_{Ce}^{'})$ and **(f)** $(6V_0^{\bullet\bullet} - 12RE_{Ce}^{'})$ occupying the first neighbor site to the associate dopant. The green sphere represents Ce^{4+} ions, red sphere represents O^{2-} ions, blue sphere represents RE^{3+} ions and black sphere represents oxygen vacancies $V_0^{\bullet\bullet}$.

Fig. 3(a) The Rietveld refined XRD patterns of GDY1 and GDY2 systems. **(b)** One of the refined output XRD pattern obtained from Rietveld refinement for the sample $y = 0.1$.

Fig. 4(a) The frequency variation of $\varepsilon'(\omega)$ for GDY1 system and in the inset for GDY2 system at temperature 525°C **(b)** The variation of dielectric constant of the co-doped samples $x = 0.05$ and $y = 0.1$ with temperature **(c)** The temperature variation of τ_{HN} for GDY1 and GDY2 system **(d)** The variation of shape parameters with temperature of the sample $y = 0.1$.

Fig. 5 The frequency dependence of dielectric loss tangent for the sample $y = 0.2$ at different temperatures. The figure in the inset shows the Arrhenius plot of $\log[T(\tan\delta_{max})]$ vs 1000/T.

Fig. 6(a) Nyquist plot for GDY1 system and in the inset for GDY2 system at temperature 525°C **(b)** The variation of grain conductivity with temperature for the sample $x = 0.05$ and $y = 0.1$.

Fig. 7 The variation of association energy and conductivity of the system **(a)** GDY1 and **(b)** GDY2.

Table I. The values of particle size (D), lattice parameter (a), RMS strain ($<\varepsilon^2>^{1/2}$), Ce–O bond length (Ce–O), weighted residual error (R_{wp}), expected error (R_{exp}) and goodness of fit (GoF) for GDY1 and GDY2. Error after forth decimal is given in the parenthesis.

Sample	D (nm)	a (Å)	$(<\varepsilon^2>^{1/2})\times10^{-4}$	Ce–O (Å)	R_{exp} (%)	R_{wp} (%)	GoF
$x = 0$	12.08	5.4146(6)	14.21	2.3442(2)	8.10	8.68	1.07
$x = 0.05$	19.36	5.4189(9)	19.96	2.3466(9)	9.47	12.26	1.29
$x = 0.1$	21.77	5.4063(2)	6.23	2.3416(1)	7.92	8.58	1.08
$y = 0$	15.08	5.4238(0)	13.10	2.3481(7)	7.54	8.43	1.12
$y = 0.1$	16.22	5.4153(7)	17.49	2.3440(2)	8.22	9.04	1.10
$y = 0.2$	13.29	5.4071(3)	15.30	2.3418(6)	8.12	8.89	1.09

Table 2. The values of unrelaxed permittivity (ε_∞), dielectric relaxation strength ($\varepsilon_s - \varepsilon_\infty$), characteristic relaxation time (τ_{HN}), shape parameters (α and β) and activation energy (E_τ) for GDY1 and GDY2 system at temperature 525℃. The errors are indicated in the parenthesis

Composition	ε_∞ (±5)	$\varepsilon_s - \varepsilon_\infty$	τ_{HN} (s)	α (±0.01)	β (±0.01)	E_τ (eV) (±0.01)
$x = 0$	736	5.13×10^4	2.4×10^{-4}	0.97	0.98	0.62
$x = 0.05$	529	2.66×10^4	1.3×10^{-4}	0.93	0.97	0.78
$x = 0.1$	323	2.82×10^4	1.0×10^{-4}	0.98	0.93	0.72
$y = 0$	320	3.03×10^4	3.0×10^{-5}	0.97	0.98	0.70
$y = 0.1$	412	5.01×10^4	4.5×10^{-5}	0.97	0.98	0.68
$y = 0.2$	190	3.00×10^4	4.0×10^{-5}	0.97	0.98	0.71

Table 3. The association energy in the temperature range 400°C-550°C (E_{asso}) and grain and specific grain boundary conductivity at 525°C of GDY1 and GDY2 system.

Sample	E_{asso} (eV) (±0.01)	σ_g ($\Omega^{-1}cm^{-1}$)	σ^s_{gb} ($\Omega^{-1}cm^{-1}$)
$x = 0$	0.04	2.05×10^{-4}	2.12×10^{-6}
$x = 0.05$	0.07	9.42×10^{-5}	9.94×10^{-7}
$x = 0.1$	0.08	1.04×10^{-4}	1.02×10^{-6}
$y = 0$	0.11	2.69×10^{-4}	2.31×10^{-6}
$y = 0.1$	0.08	3.40×10^{-4}	2.76×10^{-6}
$y = 0.2$	0.12	2.28×10^{-4}	2.08×10^{-6}

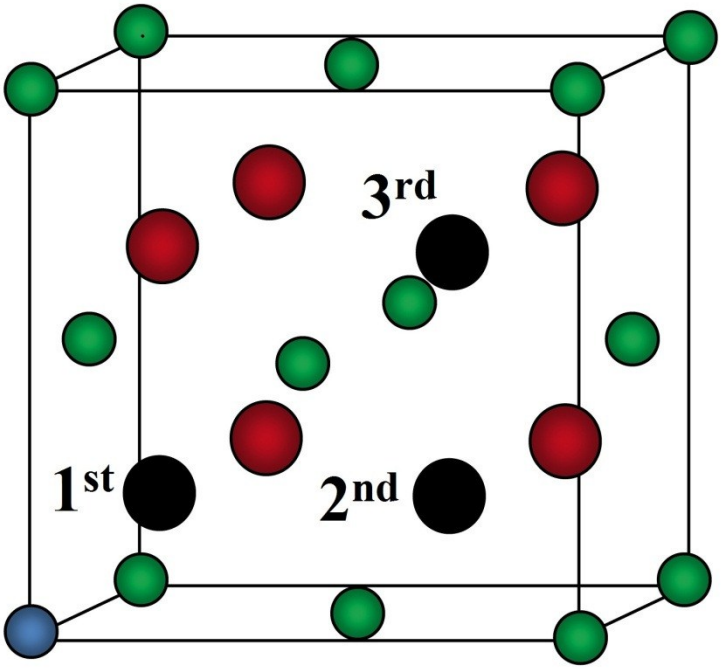

Fig. 1

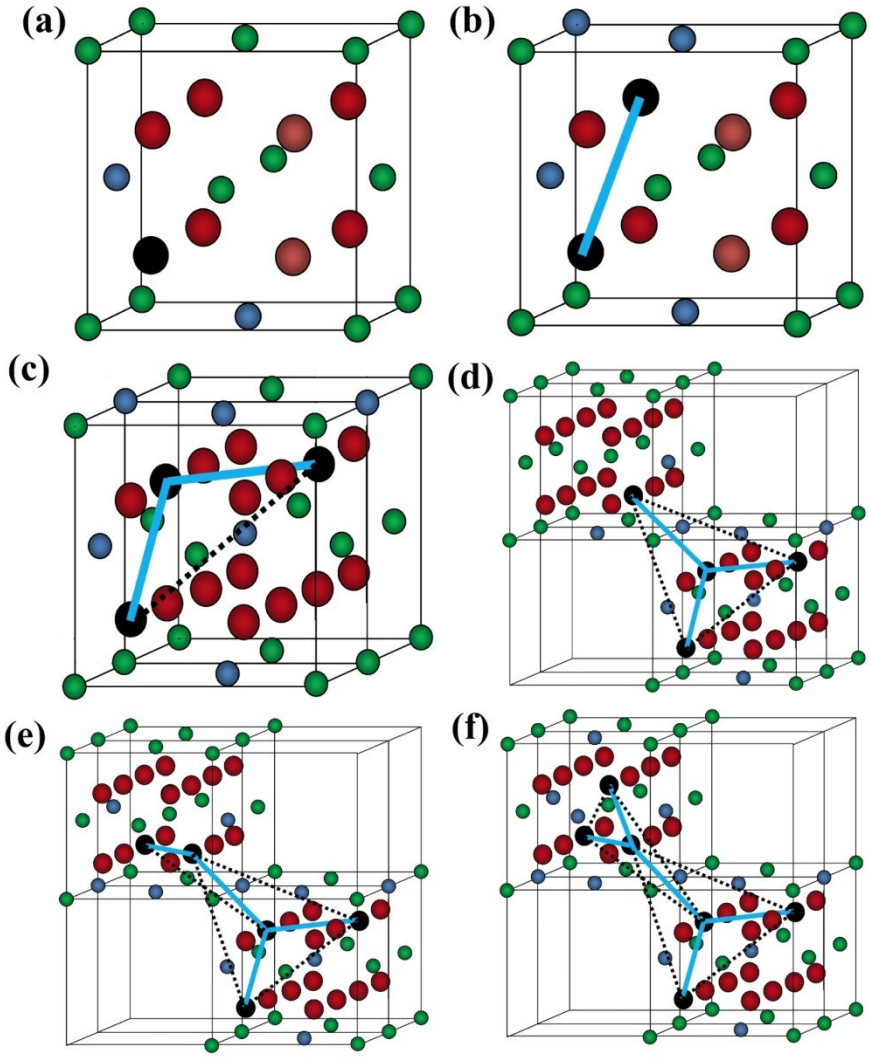

Fig. 2

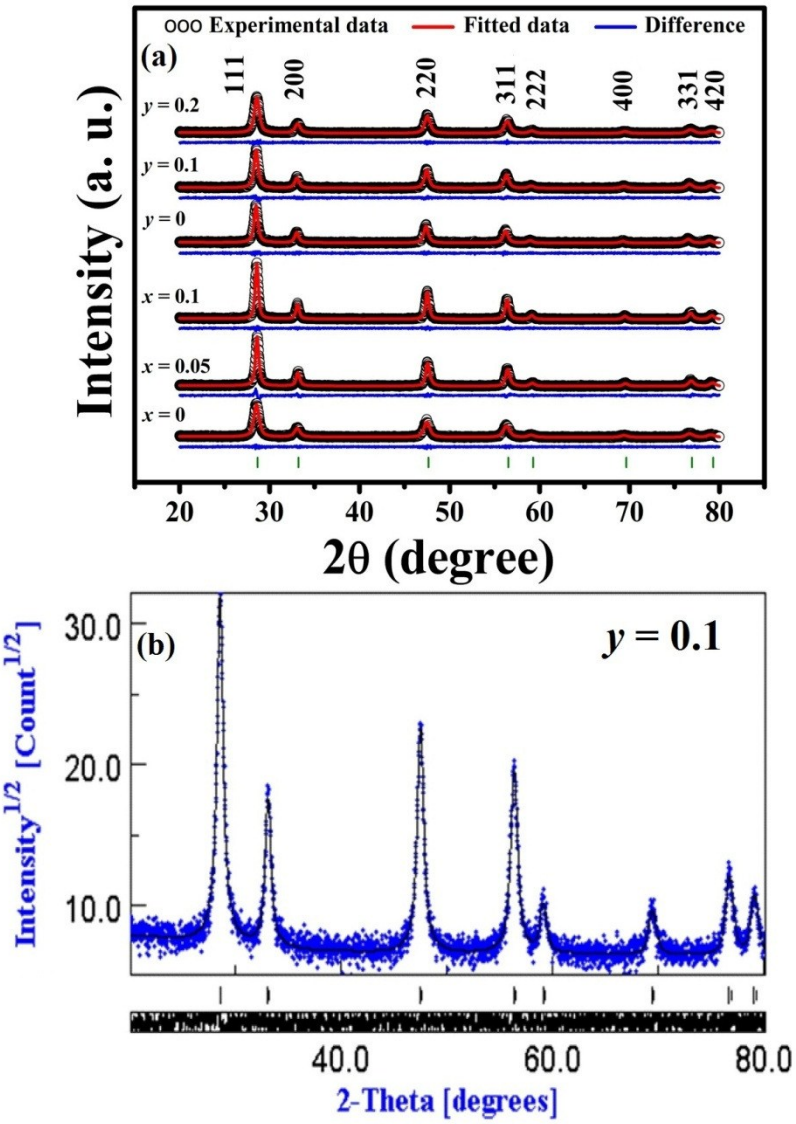

Fig. 3

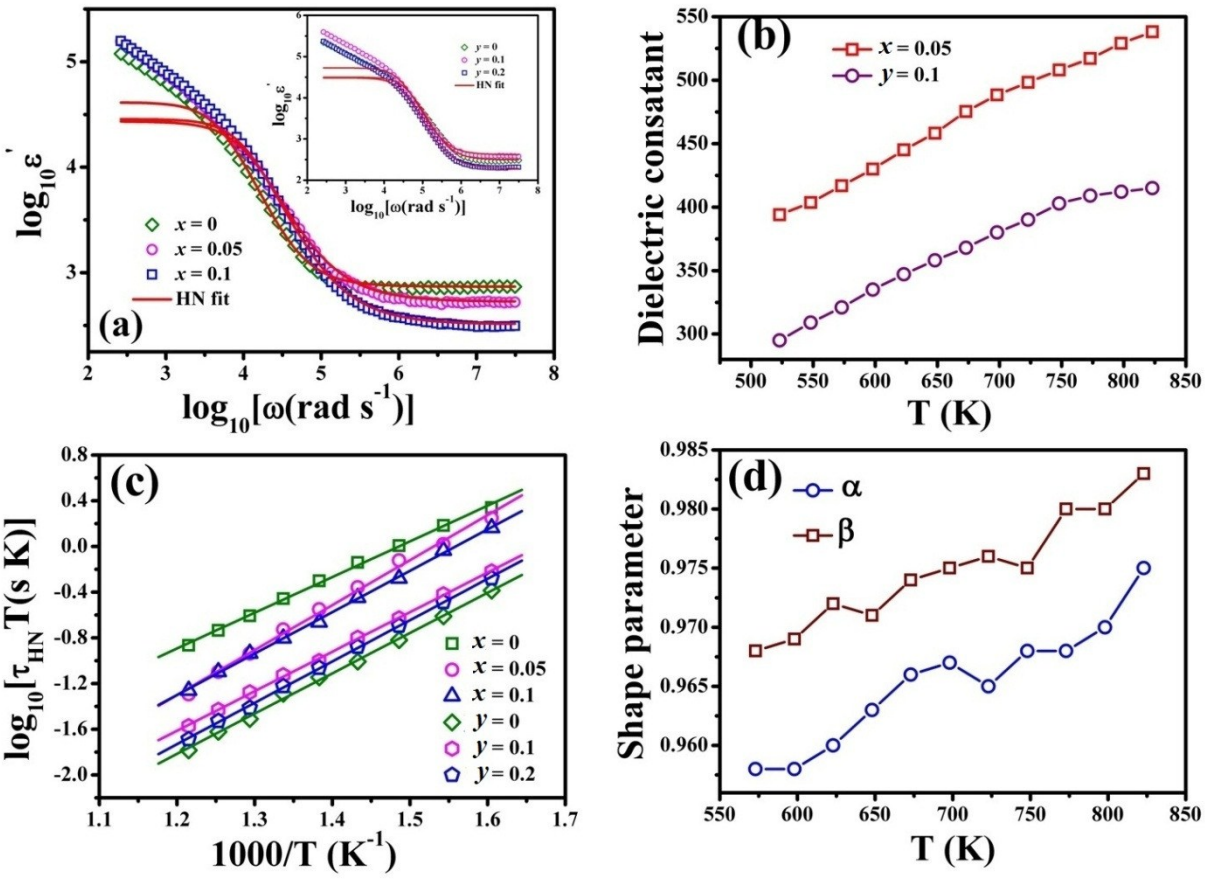

Fig. 4

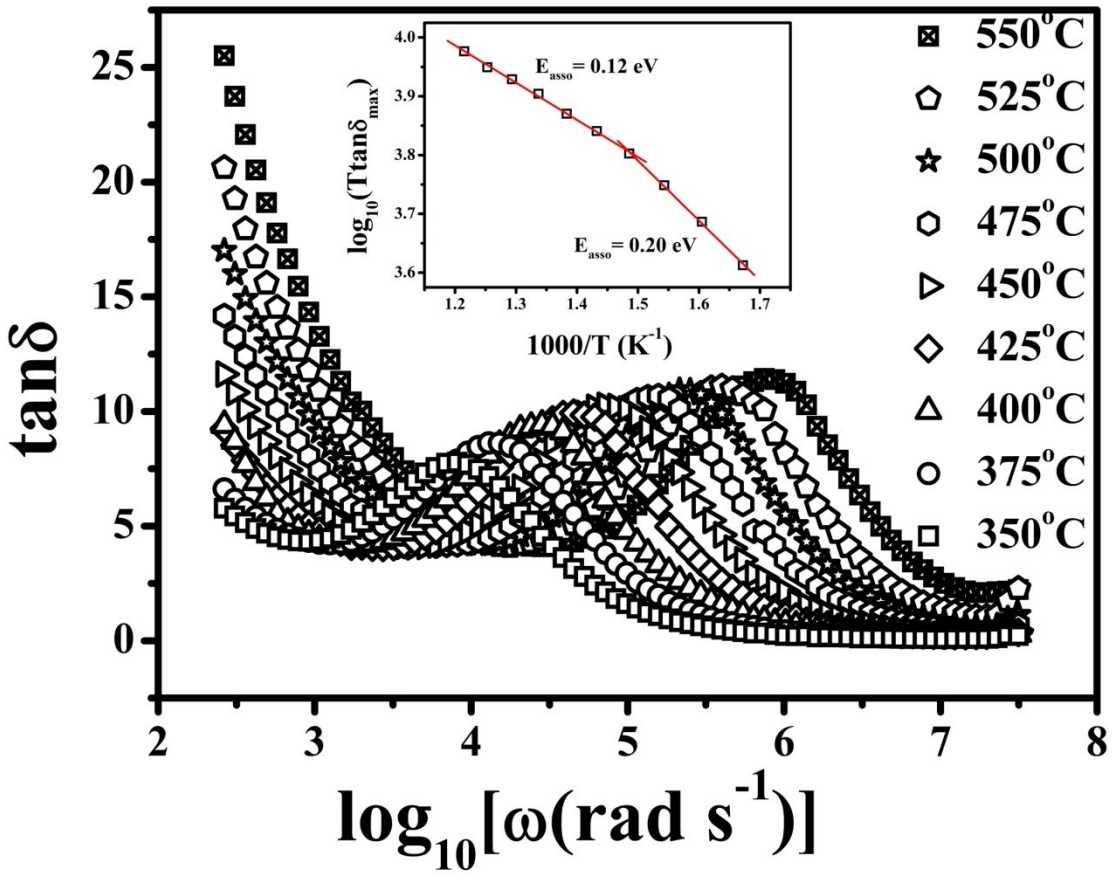

Fig. 5

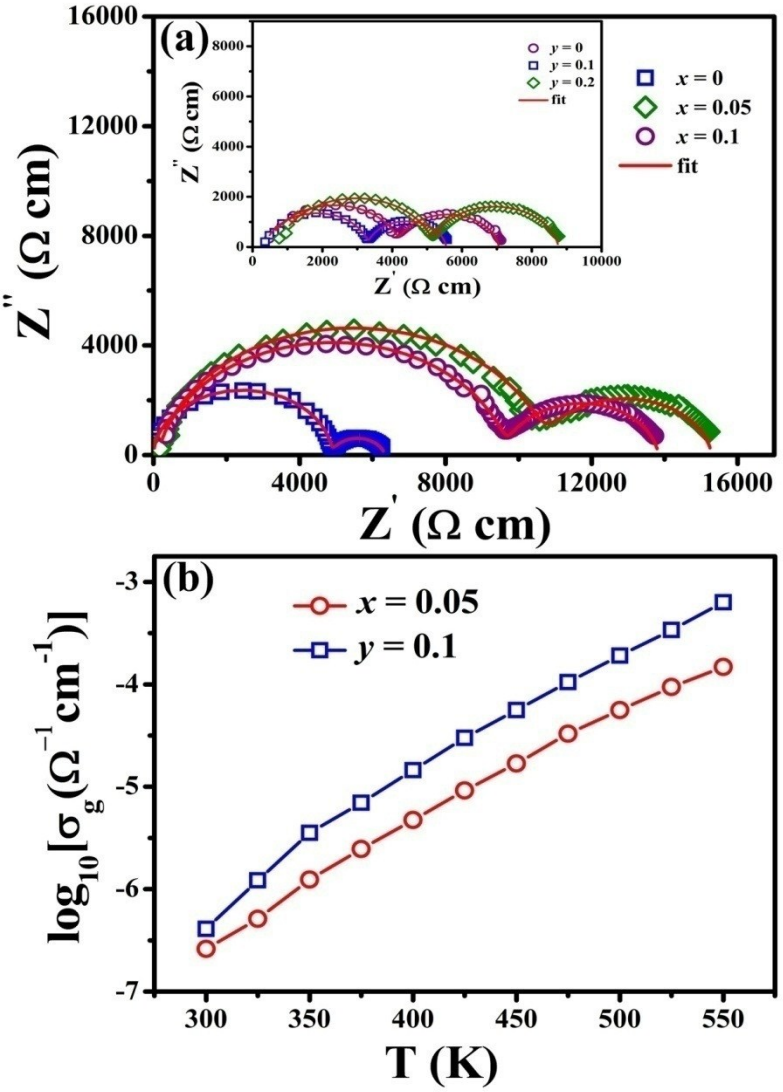

Fig. 6

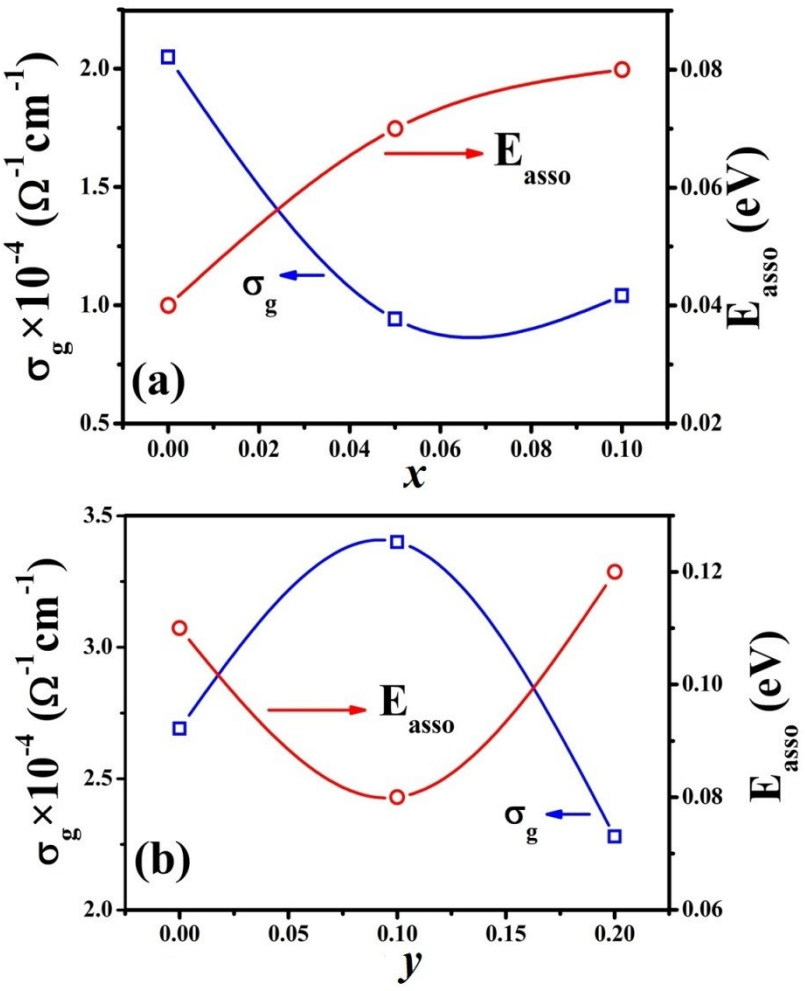

Fig. 7